Materials Today Communications 51 (2026) 114862

Contents lists available at ScienceDirect

Materials Today Communications

journal homepage: www.elsevier.com/locate/mtcomm

Comprehensive analysis of a novel iron(III) bromide based organic-inorganic hybrid material: Structural, conduction mechanisms and magnetic properties studies

Ines Khelifi [a], Khaoula Ben Brahim [a], Iheb Garoui [a], José A. Paixão [b], Noweir Ahmad Alghamdi [c], Walid Rekik [d], Rui Fausto [e,f], Abderrazek Oueslati [a,*]

[a] *Laboratory of Spectroscopic Characterization and Optical Materials, Faculty of Sciences, University of Sfax, B.P. 1171, Sfax 3000, Tunisia*
[b] *University of Coimbra, CFisUC, Department of Physics, Coimbra 3004-516, Portugal*
[c] *Departement of Physics, Faculty of Science, Alaqiq 65779, Saudi Arabia*
[d] *Laboratory Physical-Chemistry of Solid state, Chemistry Department, Faculty of Sciences of Sfax, University of Sfax, BP 1171, Sfax 3000, Tunisia*
[e] *CQC-IMS,Department of Chemistry, University of Coimbra, Coimbra 3004-535, Portugal*
[f] *Spectroscopy@IKU, Faculty of Sciences and Letters, Department of Physics, Istanbul Kultur University, Ataköy Campus, Bakirköy, Istanbul 34156, Türkiye*

ARTICLE INFO

Keywords:
Organic-inorganic hybrid material
Crystal structure
Complex impedance
CBH model
Magnetic properties

ABSTRACT

A new organic–inorganic hybrid material, $[(C_3H_7)_4N]FeBr_4$, was synthesized using the slow evaporation technique and thoroughly investigated. Its structural and physical properties were explored through single-crystal and powder X-ray diffraction, complex impedance spectroscopy, and magnetometry. Crystallographic analysis confirms that the compound adopts an orthorhombic structure, classified under the *Pbca* space group, with refined lattice parameters: $a = 14.282$ Å, $b = 16.526$ Å, and $c = 17.662$ Å. The crystal architecture features a layered configuration along the *a*-axis, consisting of alternating inorganic $[FeBr_4]^-$ anions and organic tetrapropylammonium ($[(C_3H_7)_4N]^+$) cations, arranged through electrostatic interactions. Impedance spectroscopy measurements reveal a strong dependence of the electrical response on both frequency and temperature, indicative of a relaxation mechanism driven by thermal activation. The observed negative temperature coefficient of resistance (NTCR) behavior confirms the semiconducting character of the material, with an activation energy of about 0.36 eV in the 303–363 K range. The AC conductivity behavior aligns with Jonscher's power law, supporting a hopping conduction model. Moreover, the variation of the power law exponent with temperature points to a correlated barrier hopping (CBH) mechanism, with a calculated maximum barrier energy (W_M) of 0.20 eV. Magnetic investigations show clear evidence of antiferromagnetic interactions among Fe^{3+} ions.

1. Introduction

Multifunctional materials, characterized by the coexistence of multiple physical properties (magnetic, electrical, optical, …) within a single phase, are attracting growing interest due to their strong potential in the development of devices capable of performing several functions simultaneously. Among these, organic-inorganic hybrid materials stand out due to their ability to integrate the tunability and flexibility of organic molecules with the stability and functionality of inorganic frameworks, the latter being of particular interest for magnetic transitions [1], thus enabling their widespread use in optoelectronic devices as sensors, solar cells and energy storage [2–5]. In fact, hybrid compounds with the general formula A_2MX_4 where A denotes organic cations, M is a transition metal such as Fe, Co, Cu, Mn, or Cd and X is a halogen are known to undergo multiple order-disorder structural phase transitions as commonly observed in previous studies. These transformations are primarily attributed to the dynamic reorientation and displacement of the organic parts within the crystal structure [6,7]. The latter are held together by weaker forces such as hydrogen bonds and π⋯π interactions, whereas the metal-halide components are typically linked through stronger coordinate/covalent bonds [8].

Recently, great interest has emerged for tetrapropylammonium cations $[(C_3H_7)_4N]^+$ based hybrid compounds, for example, $[(C_3H_7)_4N]_2SbCl_5$ [9], $[(C_3H_7)_4N]_2Cu_2Br_6$ [10] and $[(C_3H_7)_4N]_2Cu_2I_4$ [11], owing to their diverse properties as ferroelectricity and semiconductor behavior [12]. On the other hand, halide-iron (III) based

---

* Corresponding author.
E-mail address: oueslatiabderrazek@yahoo.fr (A. Oueslati).

https://doi.org/10.1016/j.mtcomm.2026.114862
Received 16 October 2025; Received in revised form 16 January 2026; Accepted 12 February 2026

organic inorganic hybrid compounds, like bromo-iron (III) / alkylammonium species have only been scarcely described before. Focusing on the mineral component, Shi et al. [13] conducted a comparative study on two multifunctional halide iron (III) compounds, namely tetramethylphosphonium tetrachloroferrate (III) $[(CH_3)_4N][FeCl_4]$ and tetramethylphosphonium tetrabromoferrate (III) $[(CH_3)_4N][FeBr_4]$, with the aim of exploring the impact of the anionic moiety on their magnetic properties. Since the anion directly coordinates with the Fe^{3+} center, it plays a central role in mediating magnetic interactions. Their findings demonstrated that replacing Cl^- with the larger Br^- ion significantly enhances the strength of antiferromagnetic coupling. Specifically, the $[FeBr_4]^-$ anion was found to exhibit stronger antiferromagnetic interactions than $[FeCl_4]^-$, which was attributed to differences in bond distances between the iron center and the halide ions.

Building upon recent progress in the field of hybrid materials, we report herein the synthesis of a novel iron-based organic–inorganic semiconductor with formula $[(C_3H_7)_4N]FeBr_4$. Its crystal structure was elucidated through single-crystal X-ray diffraction, while comprehensive electrical and magnetic measurements were conducted to evaluate its semiconducting behavior and magnetic response. This study underscores the potential of such metal halide hybrids in paving the way for the development of high-performance materials suitable for future electronic and spintronic applications.

2. Experimental work

2.1. Chemicals

Iron(III) bromide ($FeBr_3$, 98 % purity; FLUKA), tetrapropylammonium bromide ($[(C_3H_7)_4N]Br$, 97 % purity; FLUKA), and hydrobromic acid (HBr) were used as starting materials without further purification.

2.2. Synthesis of $[(C_3H_7)_4N]FeBr_4$

The $[(C_3H_7)_4N]FeBr_4$ hybrid compound was synthesized using a solvent evaporation method, similar to procedures previously reported for other hybrid materials [14]. The synthesis conditions were found to have a significant influence on the size and quality of the grown single crystals. The slow evaporation method was deliberately employed to achieve a controlled increase in supersaturation, thereby limiting spontaneous nucleation and promoting the growth of well-shaped crystals. In this process, a 47 % excess of hydrobromic acid was used to ensure complete dissolution of the precursors and to stabilize the bromoferrate $[FeBr_4]^-$ units in solution. This controlled acidic environment favors homogeneous crystal growth, whereas a higher acid excess may induce rapid nucleation, leading to smaller crystals or structural imperfections. Additionally, maintaining an appropriate stoichiometric ratio between the organic cation and the iron source was crucial for achieving phase purity and good crystallinity. Careful optimization of these parameters resulted in single crystals with uniform morphology and high quality, suitable for subsequent structural and physical property measurements. To achieve this, an aqueous solution was first prepared by dissolving approximately 0.1 g of $FeBr_3$ in hydrobromic acid (HBr). A stoichiometric amount of tetrapropylammonium bromide $[(C_3H_7)_4N]Br$ was then added to the solution. Red single crystals of $[(C_3H_7)_4N]FeBr_4$ of good quality formed after about 10 days of slow evaporation at room temperature. The resulting crystals were washed with absolute ethanol and dried in a vacuum desiccator. Fig. 1 presents the characteristic morphology of the $[(C_3H_7)_4N]FeBr_4$ crystalline material.

Fig. 1. Picture of $[(C_3H_7)_4N]FeBr_4$ crystals, taken under polarized light with 50 × amplification.

2.3. Single-crystal diffraction data collection and structure determination

A small single crystal of $[(C_3H_7)_4N]FeBr_4$ was carefully selected under a polarizing microscope and mounted at 296(2) K on a four-circle BRUKER APEX II area-detector diffractometer using Mo-Kα radiation ($\lambda = 0.71073$ Å). Integration and correction for Lorentz and polarization were performed using SAINT V8.38 A included in the APEX III program [15], and empirical multi-scan absorption corrections including odd and even spherical harmonics up to rank 3 and 6, respectively, were applied using the SADABS-2016/2 program [16]. The crystal structure, which belongs to the orthorhombic system with *Pbca* space group, was solved via direct methods using the SHELXT-2018 program [17] and refined by full-matrix least-square methods based on F^2 using SHELXL-2018 [18], assisted by the WINGX suite [19]. Anisotropic atomic displacement parameters were refined for all non-hydrogen atoms. All H atoms were generated geometrically using the HFIX command included in SHELXL-2018 [18] and refined using a riding model. Those involved in hydrogen bonds had the distances to their parent atoms refined within the riding model. Crystal structure illustrations were generated using the Diamond3.2 program [20]. A summary of the main crystallographic data is provided in Table1. Selected bond distances and angles, along with hydrogen-bonding interactions, are listed in Tables 2 and 3, respectively.

Table 1
Crystallographic data and structure refinements of $[(C_3H_7)_4N]FeBr_4$.

Formula	$[(C_3H_7)_4N]FeBr_4$
Color/Shape	red/block
Formula weight (g mol^{-1})	561.84
Crystal system	orthorhombic
Space group	*Pbca*
Density	1.790
Crystal size (mm)	0.150 × 0.150 × 0.150
Temperature (K)	296(2)
Diffractometer	BRUKER APEX II
a (Å)	14.282(2)
b (Å)	16.526(2)
c (Å)	17.662(2)
V (Å^3)	4168.9(10)
Z	8
Radiation type	Mo-Kα radiation
Absorption Correction	Multi-scan
θ range for data collection (°)	3.108–25.668
Measured reflections	307,474
Independent reflections	3935
Observed data [$I > 2\sigma(I)$]	1926
Index ranges	$h = -17 \rightarrow 17$
	$k = -20 \rightarrow 20$
	$l = -21 \rightarrow 21$
F(000)	2184
Number of parameters	170
R_1	0.0512
wR_2	0.1633
Goof	1.002

Table 2
Selected bond distances (Å) and angles (°).

Distances (Å)		Angles (°)	
Fe–Br2	2.3177(15)	Br3–Fe–Br4	109.43(8)
Fe–Br1	2.3182(16)	Br3–Fe–Br2	109.96(7)
Fe–Br3	2.2970(17)	Br4–Fe–Br2	107.73(7)
Fe–Br4	2.3122(17)	Br3–Fe–Br1	110.53(7)
N–C1	1.517(10)	Br4–Fe–Br1	108.86(7)
N–C4	1.518(10)	Br2–Fe–Br1	110.27(7)
N–C7	1.517(10)	C1–N–C4	110.6(6)
N–C10	1.519(10)	C1–N–C7	111.3(6)
C10–C11	1.473(13)	C4–N–C7	107.6(6)
C7–C8	1.477(12)	C1–N–C10	107.8(6)
C6–C5	1.552(12)	C4–N–C10	110.6(6)
C1–C2	1.502(12)	C7–N–C10	109.0(6)
C4–C5	1.432(12)	C11–C10–N	119.2(8)
C11–C12	1.501(13)	C8–C7–N	118.2(8)
C2–C3	1.467(13)	C2–C1–N	115.5(7)
C8–C9	1.469(12)	C5–C4–N	117.6(8)
		C10–C11–C12	109.1(9)
		C3–C2–C1	112.4(9)
		C4–C5–C6	110.7(9)
		C9–C8–C7	113.4(9)

Table 3
C–H···Br interaction geometry (Å,°).

D—H···tA	**D—H**	**H···A**	**D···A**	**D—H···A**
C10-H10B-Br4	0.97	3.10	3.875(9)	138.2
C7–H7A···Br2[i]	1.04	3.01	4.047(9)	170.3
C7–H7B···Br4	1.04	2.91	3.839(10)	149.0
C4–H4B···Br2[ii]	0.98	3.00	3.941(9)	154.4
C11–H11A···Br3[iii]	1.10	3.11	3.981(11)	137.1
C11-H11B-Br2[i]	1.10	3.14	3.881(10)	125.6

Symmetry codes:[i] $x, -y + 1/2, z + 1/2$;[ii] $x + 1/2, -y + 1/2, -z + 1$; [iii] $-x + 1/2, -y + 1, z + 1/2$

Crystallographic data for the title compound have been deposited with the Cambridge Crystallographic Data Centre under CCDC number 2466396. These data are available free of charge from the CCDC via www.ccdc.cam.ac.uk/data_request/cif.

2.4. Spectroscopic measurements

The electrical and dielectric properties of $[(C_3H_7)_4N]FeBr_4$ were investigated using impedance spectroscopy. For measurement purposes, the crystals of the compound were finely ground and pressed into a cylindrical pellet measuring 8 mm in diameter and 1 mm in thickness. To ensure good electrical contact, both surfaces of the pellet were coated with a thin layer of silver. The pellet was then positioned between two electrodes in a custom-designed measurement setup. An alternating sinusoidal voltage signal was applied across a frequency range of 40 Hz to 1 MHz. The frequency-dependent electrical and dielectric responses were recorded across a broad temperature range, from 303 K to 363 K, with measurements taken at intervals of 10 K.

2.5. Magnetic measurements

The magnetic characterization of $[(C_3H_7)_4N]FeBr_4$ was performed by VSM (Vibrating Sample Magnetometry) measurements in the temperature range 1.8–300 K and under applied magnetic fields up to 9 T. The measurements were performed on a Quantum Design Dynacool 9 T PPMS (Physical Properties Measurement System) equipped with the VSM option.

3. Results and discussion

3.1. Structure description

The newly discovered iron-based hybrid material $[(C_3H_7)_4N]FeBr_4$ adopts the orthorhombic symmetry and crystallizes at 296(2) K in the *Pbca* space group with the unit cell parameters detailed in Table1. Its structure comprises discrete $[FeBr_4]^-$ anions and $[(C_3H_7)_4N]^+$ organic cations, linked through weak C–H···Br interactions (Fig. 2).

The asymmetric unit of $[(C_3H_7)_4N]FeBr_4$, shown in Fig. 3, contains a single Fe(III) cation coordinated to four Br^- anions, as well as one independent $[(C_3H_7)_4N]^+$ organic cation. It is worth noting that all atoms occupy general positions (Wyckoff site 8*c*).

As can be seen in Fig. 3, the iron (III) cation that occupies a general position is coordinated by four bromide ions. The $[FeBr_4]^-$ complex can adopt one of three geometries: tetrahedral, square planar, or seesaw. To determine the geometry of the iron polyhedron, we calculated the τ_4 parameter ($\tau_4 = 0$ for a square plane geometry and $\tau_4 = 1$ for a tetrahedral form) using the formula [21]:

$$\tau_4 = \frac{360 - (\alpha \quad + \quad \beta)}{360 \quad - 2\theta} \tag{1}$$

Where α and β represent the two largest angles in the polyhedron, and θ is the angle in a regular tetrahedron ($\theta = 109.5°$). For our calculation, $\alpha = 110.53\,°$ and $\beta = 110.27\,°$, resulting in $\tau_4 = 0.987$. This indicates that the iron polyhedron adopts a close to ideal tetrahedral geometry.

The iron tehrahedra are stacked in such a way that they form anionic layers parallel to (1 0 0) plane at $x = ¼$ and $x = ¾$ (Fig. 2). These metal-centered tetrahedra are isolated from each other, with a shortest Fe–Fe intermetallic distance of 8.3011(19) Å. Within the $[FeBr_4]^-$ tetrahedra, Fe–Br bond lengths range from 2.2970(17) to 2.3182(16) Å, while Br–Fe–Br bond angles vary between 107.73(7) to 110.53(7) ° (Table 2).

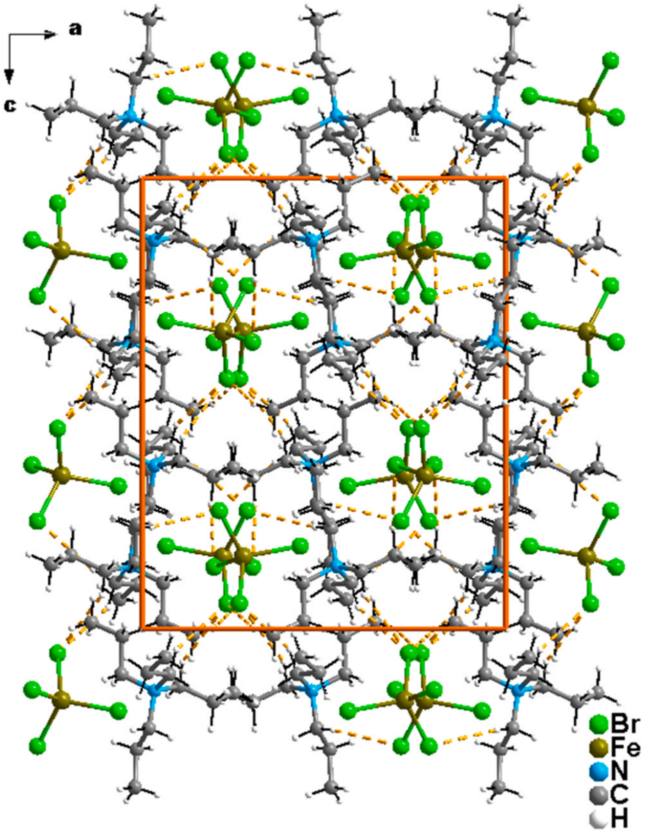

Fig. 2. Projection of the structure of $[(C_3H_7)_4N]FeBr_4$ along crystallographic *b*-axis.

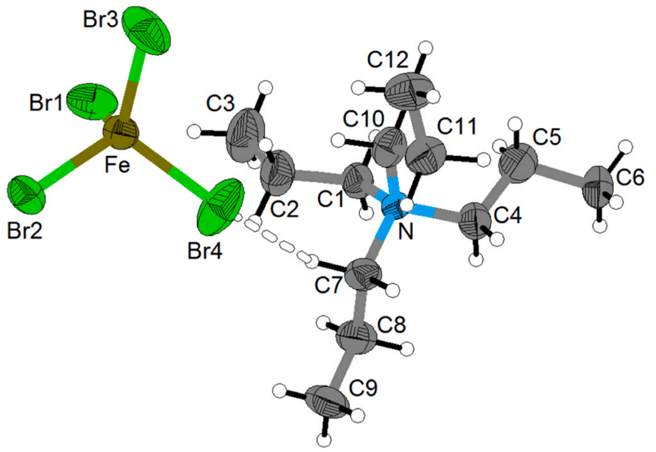

Fig. 3. The asymmetric unit of $[(C_3H_7)_4N]FeBr_4$. Displacement ellipsoids are drawn at the 50 % probability level.

These values are consistent with those reported for other compounds containing $FeBr_4$ tetrahedra [22,23]. To evaluate the geometric distortion of the $[FeBr_4]^-$ anions, the average distortion indices (DI) were calculated using the following equations [24]:

$$DI(\mathrm{Fe-Br}) = \sum_{i=1}^{n_1} \frac{|d_i - d_m|}{n_1\, d_m} \tag{2}$$

$$DI(\mathrm{Br-Fe-Br}) = \sum_{i=1}^{n_2} \frac{|a_i - a_m|}{n_2\, a_m} \tag{3}$$

Where d_i and a_i represent the individual Fe-Br bond lengths and Br-Fe-Br bond angles, respectively, and d_m and a_m are their corresponding average values. For a tetrahedral environment, $n_1 = 4$ and $n_2 = 6$.

The calculated distortion indices, DI (Fe–Br) = 0.0098 and DI (Br-Fe-Br) = 0.0072, indicate a slight deviation of the $FeBr_4$ coordination polyhedron from the ideal tetrahedral geometry. This distortion may result from the intermolecular C–H···Br interactions between the organic cations and the metallic tetrahedra identified below.

The negative charges of $[FeBr_4]^-$ tetrahedra are balanced by tetrapropylammonium cations $[(C_3H_7)_4N]^+$. The main bond lengths and angles within these organic cations, listed in Table2, are in good agreement with those found in other compounds containing the same organic cation [25,26]. These tetrapropylammonium cations $[(C_3H_7)_4N]^+$ are arranged to form organic layers parallel to (*bc*) plane at $x = 0$ and $x = ½$. Accordingly, the crystal structure can be described as an alternation of organic and inorganic layers along the crystallographic *a*-axis (Fig. 2). The connection between the organic cations and the inorganic anions is established through weak C–H···Br interactions. Indeed, each anion is connected to four tetrapropylammoniumm cations, and each organic cations is involved in C–H···Br interactions with four $[FeBr_4]^-$ anions (Fig. 4). Within these intermolecular C–H···Br interactions, the C···Br distances range from 3.839(10) to 4.047(9) Å, and the C–H···Br angles vary from 137.1 to 170.3 ° (Table3). These intermolecular C–H···Br interactions, along with van der Waals forces, play an important role in stabilizing the crystal structure by linking the organic and inorganic components.

To confirm that the single-crystal analyzed was representative of the bulk material, a powder X-ray diffractogram was collected on a polycrystalline sample consisting of fine powder obtained from grinding a few large crystals that had grown from the solution. The resulting diffractogram is shown in Fig. 5, where the measured intensities match perfectly those calculated using the structure determined from the single-crystal XRD. No further peaks assignable to impurities or extraneous phases are found in the diffractogram, confirming the high level of purity of the obtained compound.

3.2. *Electrical impedance measurements interpretation*

Electrochemical Impedance Spectroscopy (EIS) is a powerful AC-based technique widely employed to investigate the electrical properties of material–electrode interfaces, as well as the contributions to these properties originated in the material grains and grain boundaries. It operates over a broad frequency range, making it highly effective for probing charge transport and interfacial phenomena [28,29]. The complex impedance is defined by the following expression:

$$Z^*(\omega) = Z'(\omega) + jZ''(\omega) \tag{4}$$

where $Z'(\omega)$ corresponds to the real component of the impedance, indicating the resistive response of the $[(C_3H_7)_4N]FeBr_4$ material, and $Z''(\omega)$ represents the imaginary component, reflecting its capacitive characteristics [29].

Nyquist plots (Z'' vs. Z') were analyzed to evaluate the individual contributions of grains, grain boundaries, and electrode effects to the dielectric behavior and conduction mechanism of the $[(C_3H_7)_4N]FeBr_4$ system. Fig. 6 displays the Nyquist plots recorded at various temperatures. At each temperature, a well-defined semicircular arc is observed, indicative of a relaxation process, likely arising from grain interactions. As the temperature increases, the diameter of the semicircles systematically decreases, reflecting a reduction in total electrical resistance and confirming a thermally activated conduction mechanism. This

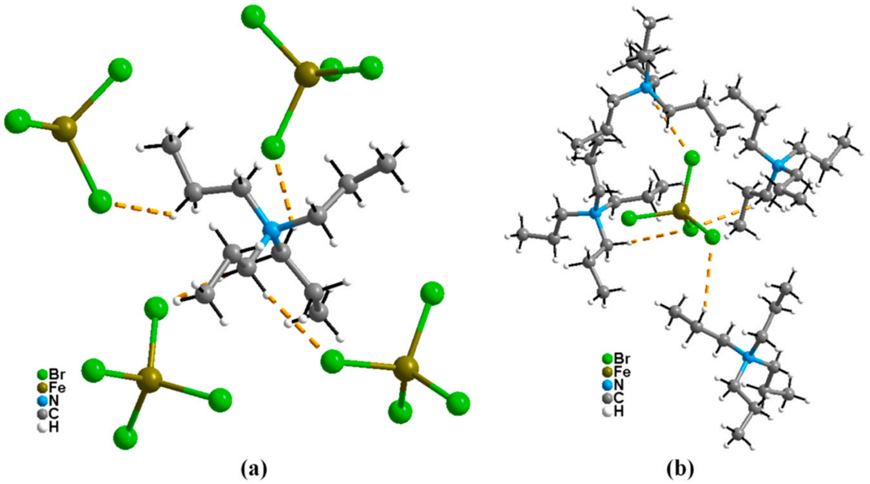

Fig. 4. Weak hydrogen bonds established by **(a)** the tetrapropylammonium cation and **(b)** $[FeBr_4]^-$ tetrahedron in $[(C_3H_7)_4N]FeBr_4$.

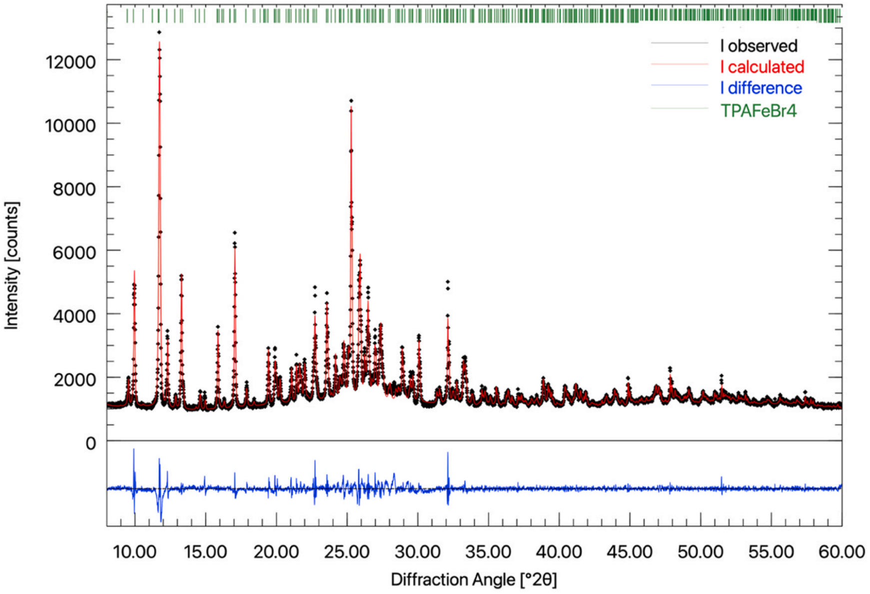

Fig. 5. Powder X-ray diffractogram of the title compound. The bottom panel shows the difference between the observed intensity and that calculated from a Rietveld refinement using the structure determined from the single-crystal XRD work using the computer program Profex5.5.1 [27]. All structural parameters were kept at the single-crystal values, only those determining the peak profiles and those modelling the sample texture were refined.

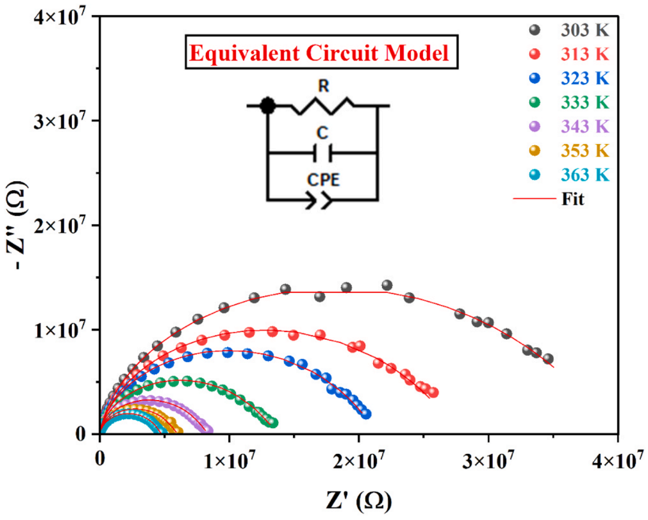

Fig. 6. Fitted Nyquist plots of $[(C_3H_7)_4N]FeBr_4$ at different temperatures using the equivalent circuit model (R//C//CPE).

temperature dependent behavior is attributed to enhanced charge carrier mobility and a possible increase in charge carrier concentration with temperature, which together contribute to improved conductivity and reduced grain boundary resistance at higher temperatures. Moreover, the observed semicircles are asymmetric and slightly depressed along the *Y*-axis, indicating a deviation from ideal Debye behavior and suggesting the presence of a non-Debye-type relaxation process in the material [30].

To further analyze the experimental $-Z''$ vs. Z' curves, the data were fitted using Z-view software [31], which enabled the extraction of a suitable equivalent circuit model (shown in the inset of Fig. 6). The fitted equivalent circuit includes a series resistor R, representing the grain resistance. This resistor is connected in parallel with a capacitor C and a constant phase element CPE, which accounts for the non-ideal capacitive behavior of the system. The constant phase element (CPE) is defined by the expression $Z_{CPE}= 1Q(j\omega)^{\alpha}$, where j is the imaginary unit, ω is the angular frequency, and α is a dimensionless exponent ranging between 0 and 1. The variation of the fitted parameters with temperature is summarized in Table 4. As shown in this table the grain resistance (R) decreases with increasing temperature, which confirms the semiconducting nature and negative temperature coefficient of resistance (NTCR) behavior of the $[(C_3H_7)_4N]FeBr_4$ material.

Fig. 7(a) shows the variation of the real part of impedance (Z') of $[(C_3H_7)_4N]FeBr_4$ as a function of angular frequency in the temperature range of 303 K to 363 K. At low frequencies, the observed decrease in Z' is attributed to a reduction in the density of trapped charges within the material [32]. This decline facilitates an increase in AC conductivity, indicating enhanced mobility of charge carriers. Such behavior suggests that charge carriers move more freely in this frequency region, improving the overall electrical conduction. At higher frequencies, the convergence of Z' values across temperatures indicates that the charge carriers possess sufficient energy to overcome potential barriers, resulting in reduced resistive effects within the material [33].

Fig. 7(b) displays the variation of the imaginary impedance component ($-Z''$) as a function of angular frequency at different temperatures. This behavior provides valuable insights into the relaxation dynamics and the underlying charge transport mechanism in $[(C_3H_7)_4N]FeBr_4$. Each spectrum reveals a well-defined peak, referred to as the "relaxation frequency." The broadening of this peak with the increase of the temperature indicates a significant deviation from ideal Debye behavior, suggesting complex dielectric relaxation within the material. At frequencies below the relaxation peak, charge transport is primarily governed by the long-range migration of charge carriers. In contrast, at frequencies above the relaxation peak the transport is dominated by localized charge carrier's motion [14]. Moreover, the observed shift of

Table 4
The electrical parameters R, C, Q, and α calculated using the Z-View software, at selected temperatures.

T (K)	R (10^6 Ω)	C (10^{-11} F)	Q (10^{-10} F)	α
303	37.976	3.182	2.903	0.69523
313	26.887	3.158	2.979	0.69928
323	20.95	3.153	2.681	0.70236
333	13.391	3.210	3.115	0.67437
343	8.2141	3.259	3.365	0.65022
353	5.9195	3.291	3.600	0.63066
363	4.6993	3.274	2.974	0.64754

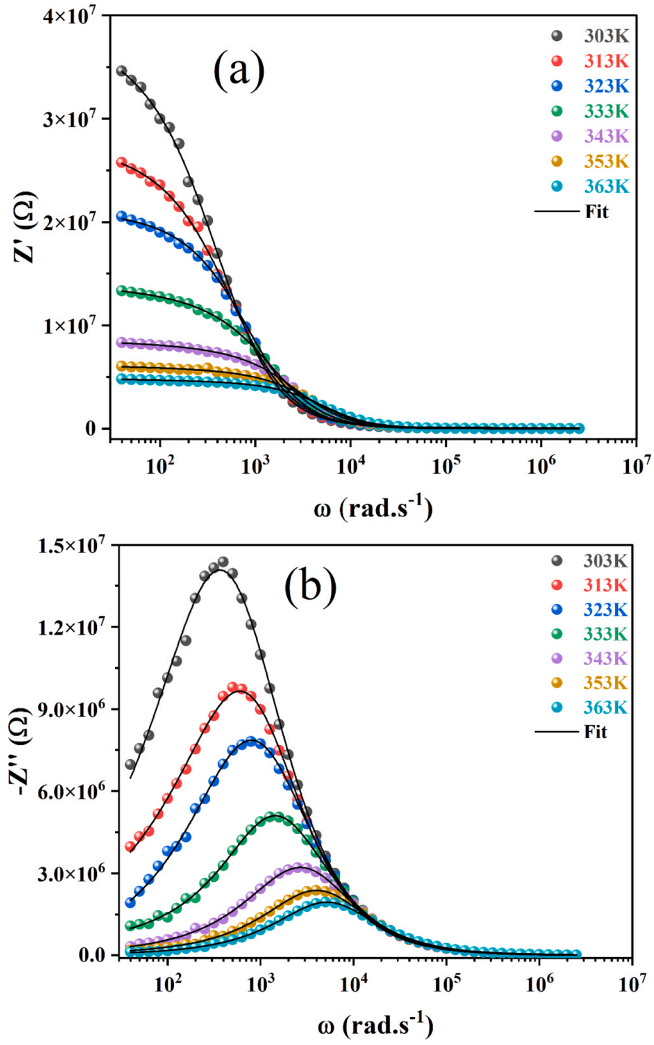

Fig. 7. (a): Temperature-dependent evolution of the real part of the complex impedance as a function of frequency. (b): Temperature-dependent evolution of the imaginary part of the complex impedance as a function of frequency.

the relaxation peak toward higher frequencies with increasing temperature confirms the thermally activated nature of the relaxation process.

To assess the theoretical impedance response, specific mathematical models [34] were employed to calculate the real and imaginary components of the complex impedance:

$$Z' = \frac{R^{-1} + Q\omega^{\alpha}\cos\left(\frac{\alpha\pi}{2}\right)}{\left(R^{-1} + Q\omega^{\alpha}\cos\left(\frac{\alpha\pi}{2}\right)\right)^{2} + \left(C\omega + Q\omega^{\alpha}\sin\left(\frac{\alpha\pi}{2}\right)\right)^{2}} \tag{5}$$

$$Z'' = \frac{C\omega + Q\omega^{\alpha}\sin\left(\frac{\alpha\pi}{2}\right)}{\left(R^{-1} + Q\omega^{\alpha}\cos\left(\frac{\alpha\pi}{2}\right)\right)^{2} + \left(C\omega + Q\omega^{\alpha}\sin\left(\frac{\alpha\pi}{2}\right)\right)^{2}} \tag{6}$$

The strong correlation between the simulated (lines in Fig. 7(a). and 7b) and experimental results (points) confirms the accuracy and appropriateness of the selected equivalent circuit model in representing the electrical behavior of the studied material.

3.3. *Electrical conductivity analysis and charge transport mechanism*

Conductivity analysis provides valuable insights into the dynamics of charge carriers, which play a central role in the overall conduction mechanism, and how their behavior evolves with temperature and frequency. As illustrated in Fig. 8, the conductivity spectra recorded over the temperature range of 303 K to 363 K exhibit two distinct regions. At low frequencies, conductivity remains nearly constant, indicating a regime dominated by direct current (DC) conduction, where mobile charge carriers are able to follow the applied electric field effectively. In contrast, at higher frequencies, a dispersion region appears, which is characteristic of alternating current (AC) conduction where the response becomes more complex due to the involvement of localized or trapped charge carriers.

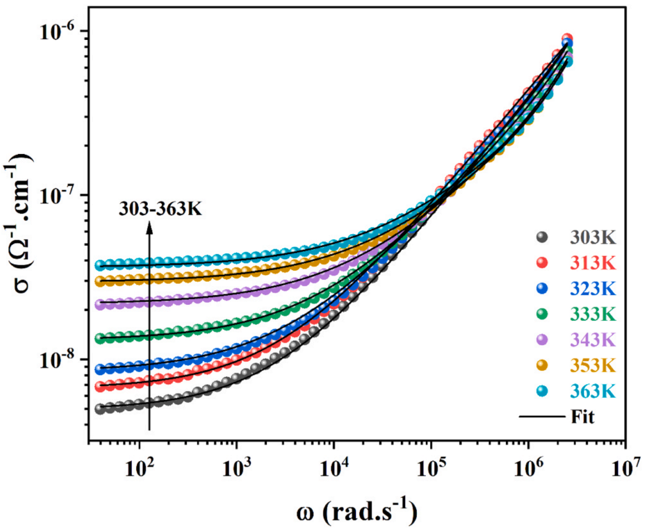

Fig. 8. Variation of the electrical conductivity of $[(C_3H_7)_4N]FeBr_4$ with frequency at various temperatures.

Moreover, at a fixed frequency, the electrical conductivity (σ) increases with rising temperature, this result being consistent with a thermally activated hopping mechanism [35]. Such behavior further confirms that charge transport in the system is primarily driven by thermal energy [36].

The phenomenon of the dispersion's conductivity is generally described by the following equation (Jonscher law) [34]:

$$\sigma_{AC}(\omega) = \frac{\sigma_s}{1+\tau^2\omega^2} + \frac{\sigma_\infty \tau^2\omega^2}{1+\tau^2\omega^2} + A\omega^s \tag{7}$$

where σ_s denotes the conductivity in the low frequency region, while σ_∞ corresponds to the estimated conductivity at high frequency limit, τ represents the relaxation time, A is a constant that varies with temperature, and $\omega = 2\pi f$ is the angular frequency. The exponent « s » shows how strongly the mobile carriers interact with the lattice, its value is usually between 0 and 1 and changes with temperature.

The DC conductivity (σ_{dc}) values at various temperatures were extracted by fitting the electrical conductivity data using the Jonscher model. The activation energy (E_a) was then calculated using the Arrhenius relation [37], based on the linear fit of the ln(σ_{dc}) vs 1000/T plot, as shown in Fig. 9.

$$\sigma_{dc} \times T = \sigma_0 \exp\left(-\frac{1000 \quad E_a}{K_B \times T}\right) \tag{8}$$

In Eq. 8, σ_0 denotes the pre-exponential factor, E_a represents the activation energy, and k_B is the Boltzmann constant. The energy activation for $[(C_3H_7)_4N]FeBr_4$ was found to be 0.36 eV in the studied temperature range.

Table 5 reveals a pronounced spread in activation energy (Ea) values among Fe^{3+}-based organic–inorganic hybrid compounds, which can be attributed to variations in structural arrangement, the size and flexibility of the organic cation, and the prevailing charge-transport processes. For the investigated $[(C_3H_7)_4N]FeBr_4$ material [38], an activation energy of 0.36 eV is obtained within the 303–363 K temperature range, placing it

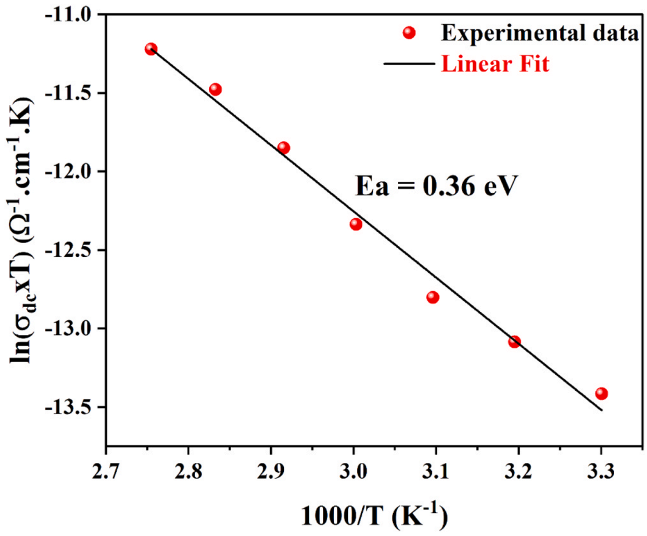

Fig. 9. Variation of $\text{Ln}(\sigma_{dc})$ versus $(1000/T)$.

Table 5
Activation energy values (Ea) reported for Fe^{3+}-based organic–inorganic hybrid materials.

Compounds	Activation Energy (eV)	Temperature (K)	References
$[(C_3H_7)_4N]FeBr_4$	0.36	303–363	This work
$[(C_3H_7)_4N]FeCl_4$	0.36–0.79	313–368	[38]
$[(CH_3)_4P]FeCl_4$	0.9–1.18	373–453	[39]
$[(C_2H_5)_4N]FeCl_4$	0.74–1.13	400–425	[40]
$[C_6H_9N_2]FeCl_4$	0.58	313–333	[41]

at the lower end of the reported values. Such a reduced Ea reflects comparatively easy charge migration, most plausibly arising from a thermally assisted hopping mechanism involving weakly localized carriers and relatively low potential barriers. By contrast, $[(C_3H_7)_4N]FeCl_4$ exhibits a wider Ea interval (0.36–0.79 eV) over a comparable temperature window, suggesting the presence of multiple transport contributions or a progressive change in the conduction regime with increasing temperature [38]. Systems containing smaller or less flexible organic cations, including $[(CH_3)_4P]FeCl_4$ [39] and $[(C_2H_5)_4N]FeCl_4$ [40], are characterized by distinctly higher activation energies (≥0.7 eV), especially at temperatures above 373 K, indicative of enhanced carrier confinement and increased energy barriers. The moderate Ea value reported for $[C_6H_9N_2]FeCl_4$ (0.58 eV) [41] further underlines the crucial role of both the organic component and the halide anion in determining transport properties. Taken together, these comparisons show that the activation energy measured in the present work places $[(C_3H_7)_4N]FeBr_4$ among the more conductive iron-based hybrid systems, while remaining in agreement with hopping-dominated conduction models commonly observed for this class of materials.

To identify the prevailing conduction mechanism in the $[(C_3H_7)_4N]FeBr_4$ compound, several theoretical models that explain the temperature dependence of the frequency exponent s in Eq. 8 can be explored [29]. As illustrated in Fig. 9, in the studied material, the exponent s decreases as temperature increases, a trend that typically indicates thermally activated hopping of localized charge carriers. This behavior strongly supports the applicability of the Correlated Barrier Hopping (CBH) model, which best describes the conduction process observed in the studied temperature range [42]. According to this model, the s can be evaluated using Eq. 9, where W_M is the self-trapping energy:

$$s = 1 - (6k_B T / W_M) \tag{9}$$

By employing Eq. 9, W_M for the studied compound was estimated to be 0.20 eV, as illustrated in Fig. 10. As $W_M \approx E_a/2$ (0.18 eV), this supports the involvement of a bi-polaron conduction mechanism [43].

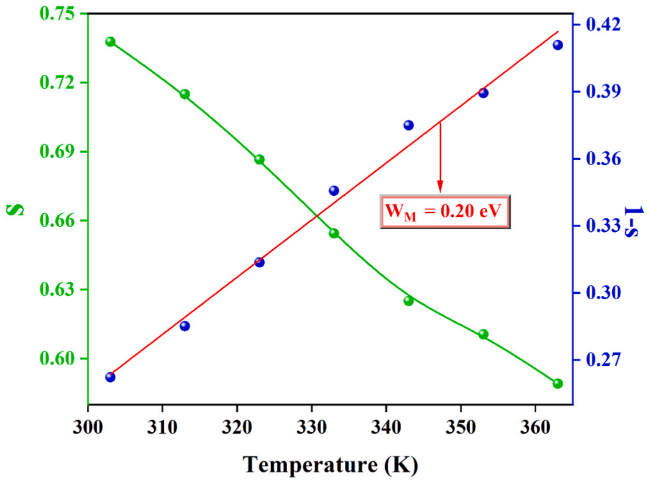

Fig. 10. The variation of the exponents (s) and (1-s) as a function of temperature.

3.4. Electrical modulus study

Studies on organic-inorganic systems have demonstrated that the electric modulus is an effective diagnostic tool for distinguishing overlapping phenomena that are otherwise obscured in impedance spectroscopy due to differences in relaxation time constants. The dielectric modulus (M^*) is defined as [44]:

$$M^* = M' + jM'' = M_\infty \left[1 - \int_0^\infty e^{-j\omega t} \left(-\frac{d\varphi(t)}{dt} \right) dt \right] \tag{10}$$

In Eq. 10, $M' = \omega C_0 Z''$ and $M'' = \omega C_0 Z'$ represent the real and imaginary components of the electric modulus, respectively, where C_0 denotes the geometrical capacitance, while $\varphi(t)$ describes the time-dependent behavior of the electric field within the material.

Fig. 11 illustrates the frequency-dependent behavior of the imaginary part of the electric modulus (M'') at temperatures ranging from 303 to 363 K. The relaxation peaks observed in $M''(\omega)$ occur in the low-frequency region (below 10^3 rad.s^{-1}) and progressively shift to higher frequencies as the temperature increases.

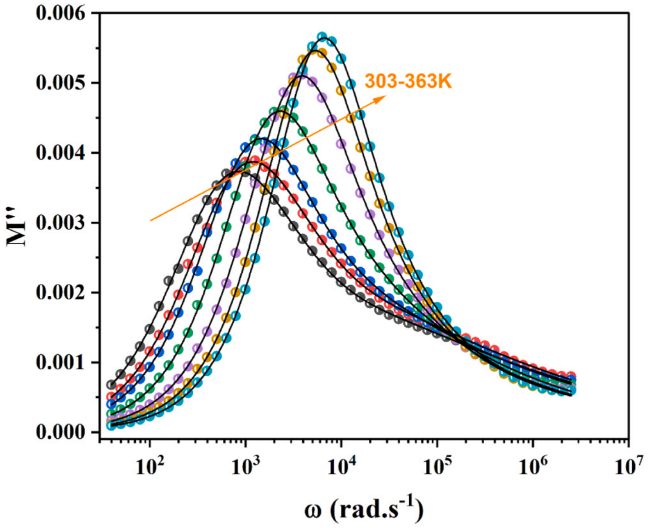

Fig. 11. Variation of the imaginary part of modulus (M'') as a function of angular frequency at various temperatures.

At low frequencies, charge carriers can move freely over longer distances (successful hopping between sites), which explains the absence of M'' peaks in this region. Conversely, in the high-frequency range, charge carriers are confined to localized motion within their potential wells. As a result, the M'' peak observed at high frequencies reflects the transition from long-range to short-range translational motion [44]. With increasing temperature, this relaxation peak shifts to higher frequencies, indicating a thermally activated dielectric relaxation process. The asymmetrical shape of the M'' peaks indicate a non-Debye relaxation behavior in the sample. To analyze this asymmetry in the imaginary part of the electric modulus, the Kohlrausch-Williams-Watts (KWW) function is utilized:

$$M''(\omega) = \frac{M''_{\max}}{\left((1-\beta) + \left(\frac{\beta}{1+\beta}\right)\right)\left[\beta\left(\frac{\omega_s}{\omega}\right) + \left(\frac{\omega}{\omega_s}\right)^{\beta}\right]} \tag{11}$$

In this expression, $M''_{\max}$ and ω_s denote the peak value of the imaginary modulus and the corresponding angular frequency, respectively. The parameter β, ranging between 0 and 1, characterizes the degree of relaxation broadening. A value of $\beta = 1$ corresponds to ideal Debye relaxation with strong dipole–dipole interactions, whereas $\beta < 1$ indicates non-Debye behavior, reflecting the presence of more complex or distributed relaxation dynamics [45].

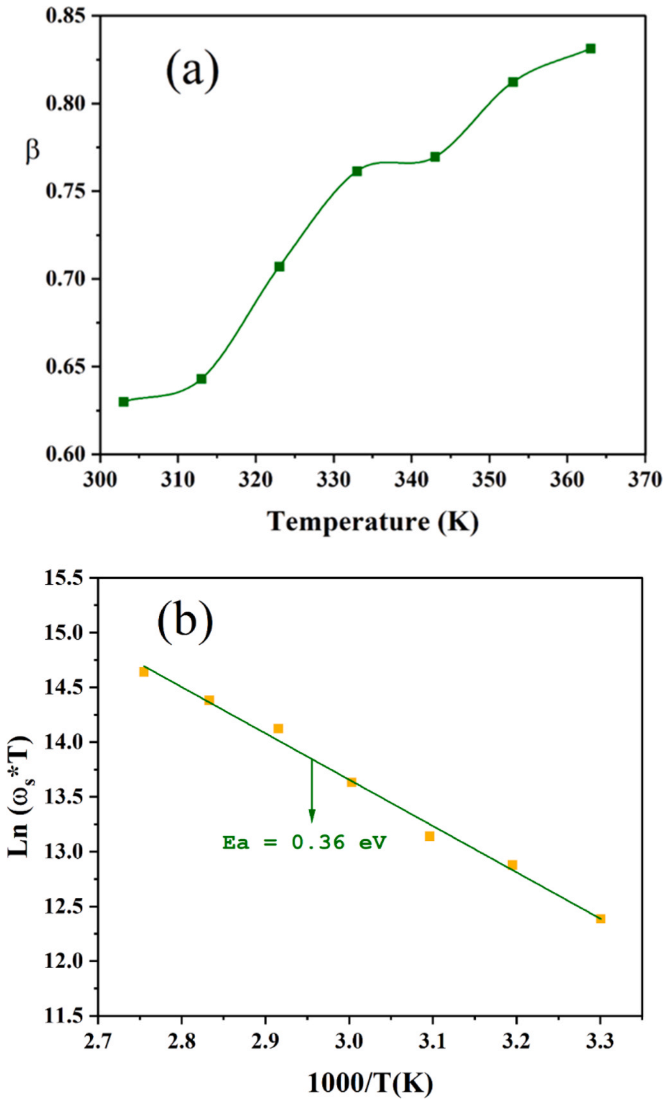

Fig. 12. **(a)**: Temperature dependence of β value. **(b)**: The variation of ln $(\omega_s T)$ versus 1000 / T.

Fig. 12(a), derived from the theoretical fit using Eq. 11, shows the temperature-dependent variation of the β parameter. The observed trend indicates that β increases with rising temperature without exceeding a value of 1, suggesting that the synthesized $[(C_3H_7)_4N]FeBr_4$ material exhibit non-Debye-type dielectric behavior.

Fig. 12(b) presents the temperature dependence of $\ln(\omega_s)$. From the linear fit, the extracted activation energy associated with the hopping process is found to be 0.36 eV. Interestingly, the activation energy Ea obtained from the modulus (M'') analysis matches that derived from conductivity measurements, indicating that the same electric parameters govern both the conduction and relaxation mechanisms in the investigated compound [37].

Fig. 13 provides a comparative analysis of Z'' and M'' as functions of angular frequency at 303 K and 363 K. The noticeable shift between the relaxation peaks of Z'' and M'' suggests a localized relaxation mechanism influenced by long-range interactions within the $[(C_3H_7)_4N]FeBr_4$ system [29,37]. As the temperature rises, this difference gradually decreases, and the peaks start to converge, indicating a transition toward a more delocalized relaxation behavior, associated with improved long-range charge mobility.

3.5. Magnetometry

A small amount (8.43 mg) of the compound in powder (polycrystalline) form was encapsulated in a low background polypropylene sample holder. Thermomagnetic measurements were performed while heating at a rate of 1 K/min after Zero Field Cooling (ZFC) followed by a Field Cooling run at the same cooling rate. Data were measured with a sample vibration amplitude and frequency of 2 mm and 40 Hz, respectively, for applied magnetic fields $B_{ap} = 0.01, 0.1, 0.5, 1.0$ and 1.5 T. The low-field ZFC and FC curves are identical and feature a clear anomaly (maximum of the susceptibility) at ~2.9 K, as depicted in Fig. 14.

Far from the anomaly, the magnetic susceptibility follows closely the modified Curie-Weiss law,

$$\chi = \frac{C}{T-\theta} + \chi_0 \tag{12}$$

where C and θ are the Curie-Weiss constant and Curie-Weiss temperature, respectively, and χ_0 accounts for a temperature independent contribution. Prior to analysis, data were corrected for the diamagnetic contribution of the sample holder and from the non-magnetic atoms using tabulated Pascal constants. An excellent fit of this law (Eq. 12) to the data with $T > 20$ K, as shown in Fig. 14, was obtained with $C = 4.328(6)\ \mathrm{cm^3 mol^{-1} K}$, $\theta = -3.12(4)$ K, $\chi_0 = -5.63(4)\mathrm{x}10^{-4}\ \mathrm{cm^3 mol^{-1}}$. The Curie-Weiss constant C corresponds to an effective magnetic moment of the Fe^{3+} atom $\mu_{eff} = 5.88\ \mu_B$, which is in good agreement with a d^5, high spin, $S = 5/2$ configuration of the transition metal ion with theoretical value of 5.92 μ_B, assuming a fully quenched orbital angular momentum. Fig. 15 shows the product $\chi_m T$ and the temperature dependent effective magnetic moment defined as $\mu_{eff}(T) = 2.82787\sqrt{(\chi_m - \chi_0) \times (T-\theta)}\ \mu_B$, as function of temperature. It can be observed that below ~20 K, deviation from Curie-law sets in, as expected from the build-up of stronger antiferromagnetic correlations between the Fe^{3+} ions that are not described accurately by this law close to and below the Néel temperature. The observed reduction of $\mu_{eff}(T)$ below ~20 K could also be due to a zero-field splitting of the d electron states, although this is expected to be a smaller effect compared to that of the antiferromagnetic exchange field for the close to ideal tetrahedral geometry of the $FeBr_4^-$ ion.

Magnetization curves (full hysteresis cycles) were measured up to 9 T for a selected range of temperatures between 2 K and 100 K (Fig. 16). Whereas the curves measured above 20 K show the expected linear behavior of a paramagnetic compound up to the maximum applied field, at lower temperatures a typical Brillouin-like shape of the $M(H)$ curves is observed between 3 K and 10 K. At the lowest

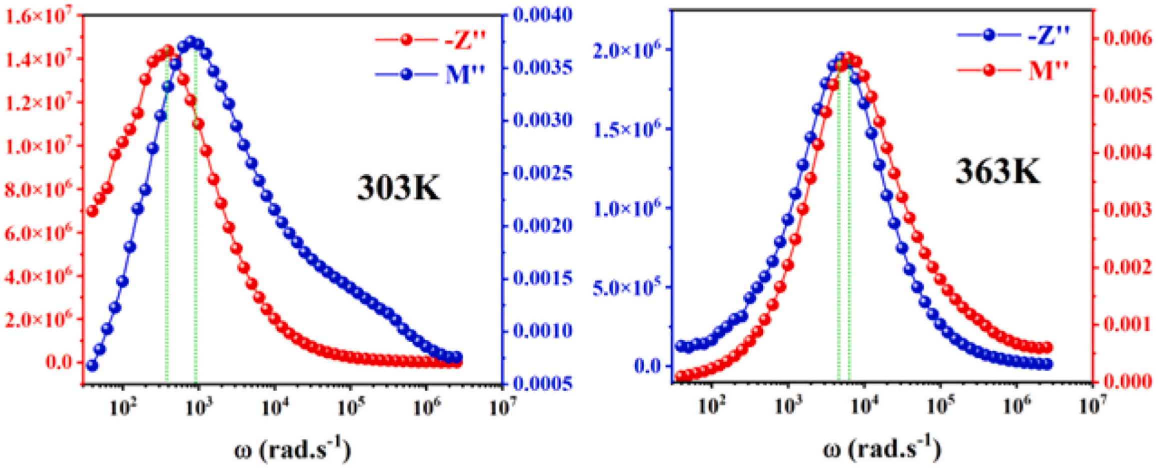

Fig. 13. Impedance and modulus spectroscopy plot at 303 K and 363 K.

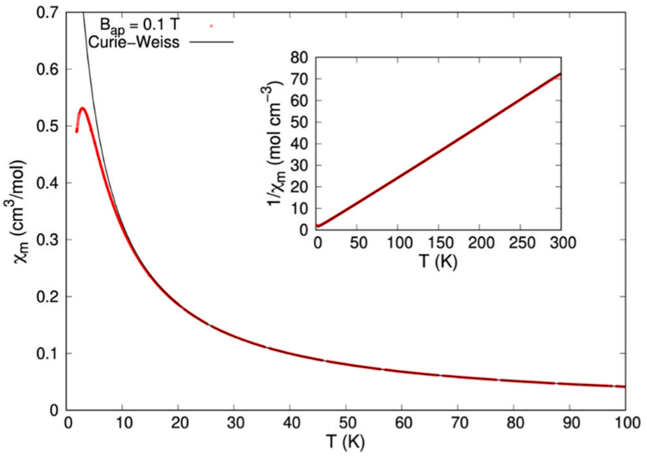

Fig. 14. Magnetic susceptibility measured on a powder sample with an applied magnetic field of 0.1 T. The solid line is the result of the fit to a modified Curie-Weiss law, using the data with $T > 20$ K. The inset shows the expected linear dependence of the inverse susceptibility as function of temperature.

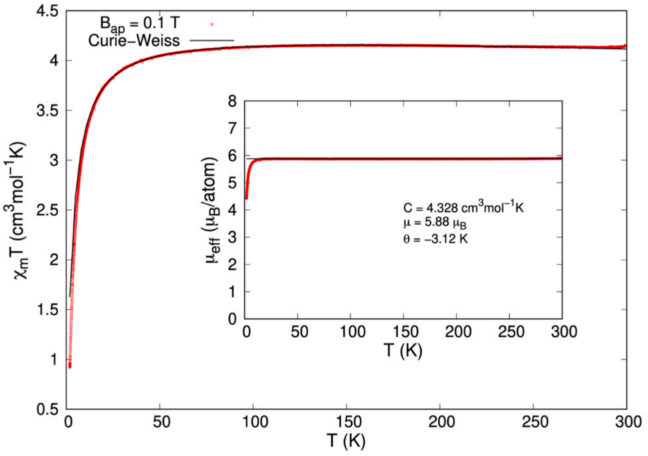

Fig. 15. Magnetic susceptibility measured with an applied magnetic field of 0.1 T. The solid line is the result of the fit to a modified Curie-Weiss law of the data with $T > 20$ K. The inset shows the effective moment as function of temperature, calculated as $\mu_{\text{eff}}(T) = 2.82787\sqrt{(\chi_m - \chi_0) \times (T - \theta)}$ μ_B, the horizontal solid line represents the value of μ_{eff} determined from the fit.

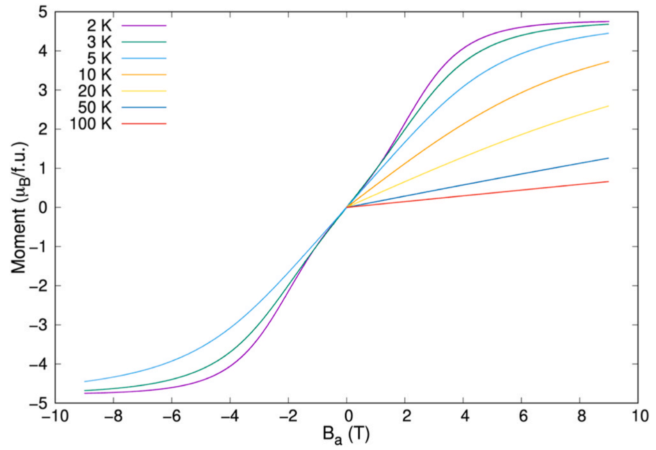

Fig. 16. Magnetization curves (expressed as magnetic moment in μ_B per formula unit) measured at a set of selected temperatures in full hysteresis cycles, with magnetic field swapped between −9 and 9 T.

temperature measured temperature of 2 K, this shape is clearly distorted from the Brillouin-like shape, as the antiferromagnetic order sets in. The magnetic moment at 2 K and 9 T appears to be close to saturation at a value of 4.75 μ_B. This is slightly reduced from the theoretical value of 5 μ_B for the $S = 5/2$ high-spin state of Fe^{3+} with $g = 2.0$. This reduction might result from a combination of crystal field and covalency effects on the metallic ion. We have tried to fit a zero-field splitting model on the Fe^{3+} ion within the weak-field (high-spin) limit with *T*d symmetry to both $\chi_M T$ and the low-temperature $M(H)$ curves, using the PHI computer code [46]. We have taken care to use proper powder averaging over a random distribution of crystallite orientations, as implemented in PHI. We have found that zero-field splitting alone cannot adequately model the observed magnetic behavior, but introducing in the model both axial zero-field splitting (D and isotropic g parameters) and an exchange parameter (zJ) a good fit could be obtained for $T > 10$ K, with $D = 5.93$ (7) cm^{-1}, $g = 1.975(1)$, $zJ = -0.121(2)$ ($\theta = -3.06$ K). Unfortunately, and as expected, a high correlation was found between the fitted parameters, so that the obtained values should be treated with caution, even if they are in the expected range of values and the $g < 2$ value is in line with the observed small reduction of the Fe^{3+} saturation moment compared to the $L = 0$, $S = 5/2$ free ion value.

4. Conclusion

In this review, particular attention is given to the characterization results of the new organic-inorganic compound $[(C_3H_7)_4N]FeBr_4$, which crystallizes in the orthorhombic system (space group *Pbca*), such that its structure is described by the tetrahedral $[FeBr_4]^-$ anions surrounded by tetrapropylammonium cations $[(C_3H_7)_4N]^+$. electric characterization shows, a frequency dependent behavior of the real (Z′) and imaginary (Z″) parts of the impedance, that was accurately modeled using an equivalent electrical circuit composed of a parallel combination of a resistance *R*, a capacitance *C* and a constant phase element CPE, reflecting the presence of a non-Debye-type relaxation process in the material behavior. Additionally, it features negative temperature coefficient of resistance (NTCR) characteristic, akin to semiconductor behavior. The AC conductivity spectra adhered to Jonscher's power law, indicating the presence of frequency dependent hopping conduction. Meanwhile, the DC conductivity followed a thermally activated Arrhenius type behavior, revealing a temperature dependence of charge carrier mobility. Thus, the variation of the "s" exponent with temperature supports the correlated barrier hopping (CBH) mechanism as the dominant charge transport process in the studied frequency and temperature range. The agreement between activation energies (~0.36 eV) obtained from DC conductivity and modulus analysis supports a common, thermally activated charge transport mechanism. Magnetic measurements confirmed that the transition metal Fe^{3+} ion is in the d^5, high field, S= 5/2 state, and that the compound displays antiferromagnetic interactions, as indicated by a Curie constant of $C = 4.328\ cm^3mol^{-1}K$ and a negative Weiss temperature ($\theta = -3.12$ K).

CRediT authorship contribution statement

Oueslati Abderrazek: Writing – review & editing, Writing – original draft, Visualization, Validation, Supervision, Resources, Methodology, Investigation, Formal analysis. **Rui Fausto:** Writing – review & editing, Writing – original draft, Supervision, Methodology. **Walid Rekik:** Writing – review & editing, Writing – original draft, Validation, Resources, Formal analysis. **Noweir Ahmad Alghamdi:** Writing – original draft, Validation, Software, Methodology. **José A. Paixão:** Writing – original draft, Validation, Software, Investigation, Formal analysis. **Iheb Garoui:** Writing – original draft, Validation, Methodology. **Khaoula Ben Brahim:** Writing – original draft, Visualization, Validation, Resources. **Khlifi Ines:** Writing – original draft, Resources, Methodology, Investigation, Formal analysis.

Declaration of Competing Interest

The authors declare that they have no known competing financial interests or personal relationships that could have appeared to influence the work reported in this paper. All persons who have participated in this work are listed as authors.

Acknowledgements

This work was partially financed through national funds by FCT - Fundação para a Ciência e Tecnologia, I.P. attributed to CFisUC in the framework of the project UID/04564/2025, with DOI identifier 10.54499/UID/04564/2025, and to the Coimbra Chemistry Centre – Institute of Molecular Sciences (CQC-IMS) through projects UIDB/00313/2025 and UIDP/00313/2025, and the IMS special complementary funds. Rui Fausto also thanks the European Union (Horizon-Widera-2023-Talents-01 ERA-Chair 1011848998 Spectroscopy@IKU "Manipulating and Characterizing Molecular Architectures: From Isolated Molecules to Molecular Crystals") for financial support.

Appendix A. Supporting information

Supplementary data associated with this article can be found in the online version at doi:10.1016/j.mtcomm.2026.114862.

Data availability

Data will be made available on request.

References

[1] A.R. Lim, Thermodynamic, physical, and structural characteristics in layered hybrid type (C2H5NH3)2MCl4 (M = 59Co, 63Cu, 65Zn, and 113Cd) crystals, Molecules 25 (8) (2020) 25081812, https://doi.org/10.3390/molecules.

[2] K. Zhou, B. Qi, Z. Liu, X. Wang, Y. Sun, et, L. Zhang, Advanced organic–inorganic hybrid materials for optoelectronic applications, Adv. Funct. Mater. 34 (52) (Déc. 2024) 2411671, https://doi.org/10.1002/adfm.202411671.

[3] Z. Ren, et al., Flexible sensors based on organic–inorganic hybrid materials, Adv. Mater. Technol. 6 (4) (2021), https://doi.org/10.1002/admt.202000889.

[4] R. Kalthoum, M. Ben Bechir, A. Ben Rhaiem, et, M.H. Dhaou, Optical properties of new organic-inorganic hybrid perovskites (CH3)2NH2CdCl3 andCH3NH3CdCl3 for solar cell applications, Opt. Mater. 125 (2022) 112084, https://doi.org/10.1016/j.optmat.2022.112084.

[5] C. Jian, et al., A thermally responsive dielectric switchable zero-dimensional organic-inorganic hybrid material: (C3H6NH2)2CoCl4, Acta Chim. Sin. 81 (5) (2023) 480, https://doi.org/10.6023/a23030064.

[6] B. Kulicka, et al., Structure, phase transitions and molecular dynamics in 4-methylpyridinium tetrachloroantimonate(III), [4-CH3C5H4NH][SbCl4, J. Phys. Chem. Solids 65 (5) (2004) 871–879, https://doi.org/10.1016/j.jpcs.2003.09.006.

[7] H.-F. Ni, et al., Molecular orientation dynamics triggers ferroelectricity and ferroelasticity in an organic–inorganic halide material, Inorg. Chem. Front 10 (24) (2023) 7231–7237, https://doi.org/10.1039/d3qi01650a.

[8] S. Dgachi, A.M. Ben Salah, M.M. Turnbull, T. Bataille, et, H. Naïli, Investigations on (C6H9N2)2[MIIBr4] halogenometallate complexes with MII = Co, Cu and Zn: Crystal structure, thermal behavior and magnetic properties, J. Alloy. Compd. 726 (2017) 315–322, https://doi.org/10.1016/j.jallcom.2017.07.278.

[9] H. Peng, et al., Bulk assembly of a 0D organic antimony chloride hybrid with highly efficient orange dual emission by self-trapped states, J. Mater. Chem. C 9 (36) (2021) 12184–12190, https://doi.org/10.1039/d1tc02906a.

[10] I. Mbarek, et al., Unraveling the properties of [TPA]2Cu2Br6: A holistic investigation into structure, optics, magnetism and dielectric characteristics, J. Mol. Struct. 1321 (2025) 140115, https://doi.org/10.1016/j.molstruc.2024.140115.

[11] H. Peng, et al., Pure white emission with 91.9% photoluminescence quantum yield of [(C3H7)4N]2Cu2I4 out of polaronic states and ultra-high color rendering index, ACS Appl. Mater. Interfaces 14 (10) (2022) 12395–12403, https://doi.org/10.1021/acsami.2c00006.

[12] M. Khalfa, et al., Synthesis, structural and electrical characterization of a new organic inorganic bromide: [(C3H7)4N]2CoBr4, RSC Adv. 12 (5) (2022) 2798–2809, https://doi.org/10.1039/d1ra07965d.

[13] P.-P. Shi, et al., Novel phase-transition materials coupled with switchable dielectric, magnetic, and optical properties: [(CH3)4P][FeCl4] and [(CH3)4P][FeBr4], Chem. Mater. 26 (20) (Oct. 2014) 6042–6049, https://doi.org/10.1021/cm503003f.

[14] I. Ibrahmi, et al., Synthesis and trigonal structure of a new lead-free zero-dimensional perovskite (CH3NH3)2[SnBr6] with multifunctional optical and electrical properties, J. Phys. Chem. Solids 207 (Dec. 2025) 112909, https://doi.org/10.1016/j.jpcs.2025.112909.

[15] Bruker, APEX2, SAINT and SADABS, Bruker AXS Inc, Madison, Wisconsin, USA, 2004.

[16] G.M. Sheldrick, SADABS Bruker AXS Inc, Madison, Wisconsin, USA, 2002.

[17] G.M. Sheldrick, SHELXT– Integrated space-group and crystal-structure determination, Acta Crystallogr. Sect. A Found. Adv. 71 (1) (Jan. 2015) 3–8, https://doi.org/10.1107/s2053273314026370.

[18] R. Herbst-Irmer, G.M. Sheldrick, Refinement of Twinned Structures with SHELXL97, Acta Crystallogr. Sect. B Struct. Sci. 54 (4) (Aug. 1998) 443–449, https://doi.org/10.1107/s0108768197018454.

[19] L.J. Farrugia, WinGXsuite for small-molecule single-crystal crystallography, J. Appl. Crystallogr. 32 (4) (Aug. 1999) 837–838, https://doi.org/10.1107/s0021889899006020.

[20] Diamond, Klaus Brandenburg. Version 3.2i, Crystal Impact GbR, Bonn, Germany, 2004.

[21] R.A. Adrian, S. Zhu, D.R. Powell, G.A. Broker, E.R.T. Tiekink, J.A. Walmsley, Dinuclear palladium(ii) complexes with bridging amidate ligands, Dalton Trans. (39) (2007) 4399, https://doi.org/10.1039/b707878a.

[22] L. Yang, D.R. Powell, et R.P. Houser, Structural variation in copper(I) complexes with pyridylmethylamide ligands: structural analysis with a new four-coordinate geometry index, τ4 », Dalton Trans. (9) (2007) 955–964, https://doi.org/10.1039/b617136b.

[23] P. González-Izquierdo, et al., Crystal and magnetic structure of the (trimim)[FeBr4] molten salt: a temperature dependence study, J. Mol. Liq. 331 (Jun. 2021) 115716, https://doi.org/10.1016/j.molliq.2021.115716.

[24] W.H. Baur, The geometry of polyhedral distortions. Predictive relationships for the phosphate group, Acta Crystallogr. Sect. B Struct. Crystallogr. Cryst. Chem. 30 (5) (May 1974) 1195–1215, https://doi.org/10.1107/s0567740874004560.

[25] N. Weslati, I. Chaabane, A. Bulou, F. Hlel, Synthesis, crystal structure, thermal and dielectric properties of tetrapropylammonium tetrachloroantimonate(III), Phys. B Cond. Matter 441 (May 2014) 42–46, https://doi.org/10.1016/j.physb.2014.02.005.

[26] I. Dhouib, H. Feki, P. Guionneau, T. Mhiri, Z. Elaoud, Structural, vibrational and thermal studies of a new nonlinear optical crystal tetrapropylammonium dihydrogenmonoarsenate bis arsenic acid, Spectrochim. Acta Part A Mol. Biomol. Spectrosc. 131 (Oct. 2014) 274–281, https://doi.org/10.1016/j.saa.2014.04.120.

[27] N. Doebelin, R. Kleeberg, Profex: a graphical user interface for the rietveld refinement programBGMN, J. Appl. Crystallogr. 48 (5) (Aug. 2015) 1573–1580, https://doi.org/10.1107/s1600576715014685.

[28] A.E. Mabrouki, O. Messaoudi, A. Dhahri, A. Azhary, M. Mansouri, L. Alfhaid, Investigation of the frequency-dependent dielectric properties of the as-prepared LaNiO3/Co3O4 nanocomposites, ACS Omega 10 (22) (Jun. 2025) 22701–22710, https://doi.org/10.1021/acsomega.4c11199.

[29] I. Garoui, et al., Dielectric relaxation and electrothermal charge carrier transport via correlated barrier hopping in the solid electrolyte TlFeP2O7: experimental and theoretical modeling, Ceram. Int. (Apr. 2025), https://doi.org/10.1016/j.ceramint.2025.04.155.

[30] S. Pujaru, P. Maji, P. Sadhukhan, A. Ray, B. Ghosh, S. Das, Dielectric relaxation and charge conduction mechanism in mechanochemically synthesized methylammonium bismuth iodide, J. Mater. Sci. Mater. Electron. 31 (11) (Apr. 2020) 8670–8679, https://doi.org/10.1007/s10854-020-03402-x.

[31] D. Johnson, ZPlot, ZView Electrochemical Impedance Software, Scribner Associates Inc, North Carolina, 2000. Version 2.3b.

[32] M. Mallek, I. Garoui, F.N. Almutairi, I. Chaabane, W. Rekik, et A. Oueslati, Synthesis, structural characterization, Hirshfeld surface analysis, and electrical properties of a zinc (II)-based organic–inorganic hybrid compound, J. Mater. Sci Mater. Electron 36 (8) (2025) 458, https://doi.org/10.1007/s10854-025-14480-0.

[33] Y. Moualhi, M. Smari, H. Nasri, et H. Rahmouni, Combined transport and dielectric models and experimental characterization based on impedance spectroscopy for studying the microstructural and transport properties of electro-ceramic perovskites, Mater. Today Commun. 38 (2024) 108529, https://doi.org/10.1016/j.mtcomm.2024.108529.

[34] I. Garoui, et al., Synthesis, crystal structure, BFDH morphology, Hirshfeld surface analysis and electrical characterization of the new bi-(2-amino-5-methylpyridinium) hexa-chlorostannate compound, Phys. E Lowdimen. Syst. Nanostruc. 158 (Apr. 2024) 115897, https://doi.org/10.1016/j.physe.2024.115897.

[35] A. Kumar, V. Saraswat, A. Dahshan, H.I. Elsaeedy, N. Mehta, Exploring dielectric and AC conduction characteristics in elemental selenium glass modified with silver halides, RSC Adv. 14 (29) (2024) 20933–20950, https://doi.org/10.1039/d4ra02999b.

[36] M.M. Fangary, M.A.O. Ahmed, The influence of frequency and temperature on the AC-conductivity in $$\text {TlInTe}_2$$ semiconductor single crystal, Sci. Rep. 15 (1) (Feb. 2025), https://doi.org/10.1038/s41598-025-87788-w.

[37] I. Garoui, M. Mallek, F.N. Almutairi, W. Rekik, A. Oueslati, Synthesis, structural characterization and complex impedance analysis of a novel organic-inorganic hybrid compound based on Mercury (II) chloride, J. Mol. Struct. 1315 (Nov. 2024) 138881, https://doi.org/10.1016/j.molstruc.2024.138881.

[38] Kh. Ben Brahim, M.Ben gzaiel, A. Oueslati, F. Hlel, M. Gargouri, Synthesis, structural characterization and electrical conduction mechanism of the new organic–inorganic complex: ([(C3H7)4N]FeCl4), Mater. Res. Bull. 118 (Oct. 2019) 110505, https://doi.org/10.1016/j.materresbull.2019.110505.

[39] M. Ben Gzaiel, K. Khirouni, M. Gargouri, Optical and electrical studies on the semiconductor compound for the photovoltaic applications, J. Organomet. Chem. 950 (Oct. 2021) 121992, https://doi.org/10.1016/j.jorganchem.2021.121992.

[40] Kh. Ben Brahim, M. Ben gzaiel, A. Oueslati, M. Gargouri, Electrical conductivity and vibrational studies induced phase transitions in [(C2H5)4N]FeCl4, RSC Adv. 8 (71) (2018) 40676–40686, https://doi.org/10.1039/c8ra07671e.

[41] A. Ghoudi, et al., Crystal structure and optical characterization of a new hybrid compound, C6H9N2FeCl4, with large dielectric constants for field-effect transistors, RSC Adv. 13 (19) (2023) 12844–12862, https://doi.org/10.1039/d3ra01239e.

[42] G.E. Pike, AC conductivity of scandium oxide and a new hopping model for conductivity, Phys. Rev. B 6 (4) (Aug. 1972) 1572–1580, https://doi.org/10.1103/physrevb.6.1572.

[43] I. Garoui, et al., New organic–inorganic chloride (2-amino-4-methylpyridinium hexachlorostannate): Crystal structure, BFDH morphology, and electrical conduction mechanism, J. Phys. Chem. Solids 206 (Nov. 2025) 112840, https://doi.org/10.1016/j.jpcs.2025.112840.

[44] A. Molak, M. Paluch, S. Pawlus, J. Klimontko, Z. Ujma, I. Gruszka, Electric modulus approach to the analysis of electric relaxation in highly conducting (Na0.75Bi0.25)(Mn0.25Nb0.75)O3ceramics, J. Phys. D Appl. Phys. 38 (9) (Apr. 2005) 1450–1460, https://doi.org/10.1088/0022-3727/38/9/019.

[45] S. Chkoundali, I. Garoui, W. Trigui, A. Oueslati, Crystal structure, hirshfeld surface analysis, conduction mechanism and electrical modulus study of the new organic–inorganic compound [C8H10NO]2HgBr4, RSC Adv. 14 (13) (2024) 8971–8980, https://doi.org/10.1039/d4ra00689e.

[46] N.F. Chilton, R.P. Anderson, L.D. Turner, A. Soncini, K.S. Murray, PHI - a powerful new program for the analysis of anisotropic monomeric and exchange-coupled polynuclear d- and f-block complexes, J. Comput. Chem. (2013) 1164–1175, https://doi.org/10.1002/jcc.23234.